

# Distinguishing GR and $f(R)$ gravity with the gravitational lensing Minkowski Functionals

Chenxiaoji Ling,<sup>1</sup> Qiao Wang,<sup>1</sup> Ran Li,<sup>1</sup> Baojiu Li,<sup>2</sup> Jie Wang,<sup>1</sup> and Liang Gao<sup>1,2</sup>

<sup>1</sup>National Astronomical Observatories, Chinese Academy of Sciences, 20A Datun Road, Chaoyang, Beijing 100012, China

<sup>2</sup>Institute for computational Cosmology, Department of Physics,  
Durham University, South Road, Durham DH1 3LE, UK

(Dated: April 17, 2019)

We explore the Minkowski Functionals of weak lensing convergence map to distinguish between  $f(R)$  gravity and the General Relativity (GR). The mock weak lensing convergence maps are constructed with a set of high-resolution simulations assuming different gravity models. It is shown that the lensing MFs of  $f(R)$  gravity can be considerably different from that of GR because of the environmentally dependent enhancement of structure formation. We also investigate the effect of lensing noise on our results, and find that it is likely to distinguish F5, F6 and GR gravity models with a galaxy survey of  $\sim 3000$  degree<sup>2</sup> and with a background source number density of  $n_g = 30$  arcmin<sup>-2</sup>, comparable to an upcoming survey Dark Energy survey (DES).

PACS numbers: 04.50.Kd,95.30.Sf,95.36.+x,98.65.Dx

## I. INTRODUCTION

It is fundamentally important to explain the observed accelerating expansion of the Universe [1, 2]. In the current understanding, this accelerating expansion either is driven by an exotic dark energy in the framework of general relativity (hereafter GR) or indicates that GR needs to be modified on large scales [3]. A well-studied example of the latter scenario is the so-called  $f(R)$  gravity [4], in which the Ricci scalar  $R$  in the standard Einstein-Hilbert action is replaced by a function  $f(R)$ . In most  $f(R)$  models studied so far, the difference between  $f(R)$  and  $R$  remains roughly a constant through out the cosmic history, therefore accelerating the expansion of the Universe like in the standard  $\Lambda$ CDM paradigm.

Although the background expansion history in  $f(R)$  models could be practically indistinguishable from that of  $\Lambda$ CDM, the structure formation can be very different for these two scenarios. In  $f(R)$  gravity,  $df/dR$  is nontrivial and behaves like a dynamical scalar field, which propagates a ‘fifth force’ between matter particles. The strength of this fifth force can be maximally 1/3 of that of Newtonian gravity, but it is usually weaker because of the well-known chameleon mechanism [5], which strongly suppresses it in regions with high matter density (or deep gravitational potential). The idea is that any deviation from standard GR gravitational law would be ‘screened’ and therefore undetectable in the solar system, in which the validity of GR has been confirmed experimentally to very high precision. However, it is worth stressing that the behaviour of the fifth force in solar-like systems relies heavily on what is going on at much larger scales such as the Milky Way galaxy, its dark matter halo and beyond. Although recent works have demonstrated the encouraging potential of constraining  $f(R)$  gravity using such systems, [6, 7], better understandings of the large-scale behaviour of the scalar field will be needed before quantitative conclusions are finally drawn. In this sense, it is crucial to study the cosmological behaviour of  $f(R)$  gravity, as a means to constrain gravity using the constantly improving cosmological data (see [8] for a recent review).

Previous works on this subject using statistics of large scale structure often compare matter power spectrum and correla-

tion functions of matter distribution in GR and  $f(R)$  gravity [see, e.g., 9–12]. In this work, we investigate the topological difference in the lensing convergence  $\kappa$  map between GR and  $f(R)$  universes. The lensing  $\kappa$  map reflects the projected mass distribution of the Universe; its topological information can be described using Minkowski functionals (MFs) [13, 14]. In recent works, MFs have been extensively used to study the geometry properties of cosmic field ([15–20]). It’s been shown that lensing MFs contain significant information beyond other statistical quantities, e.g. the power spectrum [21], thus might provide a promising way to distinguish  $f(R)$  and GR model.

In this paper, we construct mock lensing maps with a set of  $f(R)$  and GR cosmological simulations using the ECOSMOS [22] code, and investigate whether or not the MFs of lensing map can be used to distinguish different gravity models.

This paper is organised as follows. In section 2, we briefly introduce the general  $f(R)$  models and the  $N$ -body simulations used in this work. In section 3, we present our algorithm to calculate the MFs. In section 4 we present our results, and we give a summary in section 5.

## II. THE $f(R)$ COSMOLOGY

### A. The $f(R)$ gravity model

The  $f(R)$  gravity model is a simple generalisation of standard  $\Lambda$ CDM paradigm by replacing the Ricci scalar  $R$  in the Einstein-Hilbert action with an algebraic function of  $R$ . The modified action can be written as:

$$S = \int d^4x \sqrt{-g} \left\{ \frac{M_{Pl}^2}{2} [R + f(R)] + \mathcal{L}_m \right\}, \quad (1)$$

in which  $M_{Pl}$  is the reduced Planck mass,  $M_{Pl}^{-2} = 8\pi G$ ,  $G$  is Newton’s constant,  $g$  is the determinant of the metric  $g_{\mu\nu}$  and  $\mathcal{L}_m$  is the Lagrangian density for matter fields.

There is plenty of literature about the derivation and properties of the modified Einstein equations in  $f(R)$  gravity, and here we shall not repeat the details. Instead, we simply present

the equations that are directly relevant to the cosmic structure formation. These are the modified Poisson equation:

$$\nabla^2 \Phi = \frac{16\pi G}{3} a^2 \delta \rho_m + \frac{a^2}{6} \delta R(f_R), \quad (2)$$

and the equation of motion (EoM) of the scalar field  $f_R \equiv df(R)/dR$ :

$$\nabla^2 f_R = -\frac{a^2}{3} [\delta R(f_R) + 8\pi G \delta \rho_m], \quad (3)$$

in which

$$\delta R \equiv R - \bar{R}, \quad \delta \rho_m \equiv \rho_m - \bar{\rho}_m. \quad (4)$$

$\Phi$  denotes the gravitational potential,  $\rho_m$  is the total density of matter (cold dark matter and baryons), and an overbar denotes the background average.  $a$  is the cosmic scale factor and  $a = 1$  at present.

The  $f(R)$  model has a GR limit, which is given by  $f_R \rightarrow 0$ . In this limit, the scalar field  $f_R$  becomes nondynamical (identically zero); Eq. (3) gives the GR relation  $\delta R = -8\pi G \delta \rho_m$  and Eq. (2) reduces to the standard Poisson equation:

$$\nabla^2 \Phi = 4\pi G a^2 \delta \rho_m. \quad (5)$$

For general  $f(R)$  gravity, on the other hand, the scalar field  $f_R$  has a complicated behaviour, and leads to an environmentally dependant effective Newton's constant  $G_{\text{eff}}$ .

As described in the introduction, local tests of gravity based on solar system observations put a tight constraint on any deviation from the Newtonian gravity. The chameleon mechanism is introduced to evade the constraint by varying  $G_{\text{eff}}$  in different environments. In dense regions,  $\delta f_R$  becomes negligible, and one has

$\delta R(f_R) \approx -8\pi G \delta \rho$ , thus Eq. (2) returns to the GR equation, Eq. (5). In under-dense environments, the  $\delta R(f_R)$  term in Eq. (2) becomes small and the Eq. (2) turns into:

$$\nabla^2 \Phi = \frac{16}{3} \pi G a^2 \delta \rho, \quad (6)$$

where the effective Newton's constant is enhanced by a factor of 1/3 ( $G_{\text{eff}} = 4G/3$ ) compared to its value in dense environments.

Note that the maximum enhancement of  $G$  in  $f(R)$  gravity is always 1/3, independent of the functional form of  $f(R)$ .  $f(R)$ , on the other hand, determines how  $G_{\text{eff}}$  changes from  $G$  to  $4G/3$  when environmental density changes. Therefore, the form of  $f(R)$  is crucial for a given model. To date, various  $f(R)$  functions have been designed to explain the accelerated cosmic expansion while evading solar system constraints, of which the most well-studied is the one proposed by [23]:

$$f(R) = -M^2 \frac{c_1 (-R/gM^2)^n}{c_2 (-R/M^2)^n + 1}, \quad (7)$$

where  $M^2 \equiv H_0^2 \Omega_m$  with  $H_0$  the Hubble constant,  $\Omega_m$  is the matter density parameter, and  $n$  is an integer parameter which is normally set to 1, though other values have been studied as well. To match<sup>1</sup> the expansion of a standard  $\Lambda$ CDM universe, the dimensionless parameters  $c_1$  and  $c_2$  should satisfy:

$$\frac{c_1}{c_2} = 6 \frac{\Omega_\Lambda}{\Omega_m}, \quad (8)$$

where  $\Omega_\Lambda$  is the current dark energy density parameter.

In any reasonable cosmological model, we have  $-\bar{R} \gg M^2$ , and so  $\bar{f}_R$  can be simplified as:

$$f_R \simeq -\frac{nc_1}{c_2^2} \left( \frac{M^2}{-R} \right)^{n+1}. \quad (9)$$

Therefore, the model can be described by two free parameters,  $n$  and  $c_1/c_2^2$ , and the latter is determined by  $f_{R0}$ , the value of  $f_R$  today.

## B. Numerical simulations

Numerical simulations used in this study include three high resolution cosmological  $N$ -body simulations, two of which assume  $f(R)$  gravity and one assumes  $\Lambda$ CDM. For two different  $f(R)$  simulations, we have fixed the model parameter  $n$  to be 1 but varied the parameter  $f_{R0}$  by  $|f_{R0}| = 1.289 \times 10^{-5}$  and  $1.289 \times 10^{-6}$ , which will hereafter be referred to as F5 and F6 model, respectively. All simulations evolve  $1024^3$  particles in a  $250 h^{-1} \text{Mpc}$  cubic volume and start from exactly the same initial conditions at  $z = 49.0$ . The simulations were performed with the adaptive mesh refinement code ECOSMOG [22]. The cosmological parameters assumed to generate initial conditions are  $\Omega_m = 0.267$ ,  $\Omega_\Lambda = 0.733$ ,  $h = 0.71$ ,  $n_s = 0.958$  and  $\sigma_8 = 0.801$ , in which  $h = H_0/(100 \text{km/s/Mpc})$ ,  $n_s$  is the spectral index of the primordial power spectrum and  $\sigma_8$  is the RMS density fluctuation within spherical tophat windows of radius  $8 h^{-1} \text{Mpc}$ . In this work, we use the snapshot at  $z \approx 0.1$  to construct lensing  $\kappa$  maps.

## III. THE MINKOWSKI FUNCTIONALS (MFS) OF WEAK LENSING $\kappa$ MAP

### A. Weak lensing convergence map

Weak lensing observations measure small distortions on the shapes of background galaxies, which can be used to generate convergence  $\kappa$  map. The convergence map  $\kappa(\mathbf{x})$  is related to projected density map  $\Sigma(\mathbf{x})$  as:

$$\kappa(\mathbf{x}) = \frac{\Sigma(\mathbf{x})}{\Sigma_{cr}}, \quad (10)$$

<sup>1</sup> We note that this is an approximate match, with an error of order  $f_R$ , which is practically too small to be observable. As mentioned earlier, it is possible to have an exact  $\Lambda$ CDM expansion history in  $f(R)$  gravity, but the corresponding form of  $f(R)$  is more complicated.

with the critical surface density

$$\Sigma_{cr} = \frac{c^2}{4\pi G} \frac{D_s}{D_l D_{ls}}, \quad (11)$$

in which  $D_{ls}$  is the angular diameter distance between source galaxies and the lens, and  $D_l$  and  $D_s$  are the angular diameter distances from the observer to the lens and to the sources.  $c$  is the speed of light.

To generate a theoretical convergence map, we project particles in the whole simulation box onto a plane. Next we employ the cloud in cell (CIC) method to project dark matter particles to a  $5000^2$  grid surface density map. On average, there are about 43 particles on each grid, the grid separation is about  $50 h^{-1} \text{kpc}$ . Then we convert the surface density map to convergence map by assuming our lens plane to be at  $z = 0.1$ , and all source galaxies at redshift  $z = 1$ . The total sky area of our mock lensing observation is about  $3000 \text{ degree}^2$ , comparable to forthcoming dark energy surveys (e.g., LSST [24] and Euclid [25]).

In real observations, the intrinsic ellipticity of source galaxies introduces noise to the convergence map. The Gaussian smoothing is often adopted to suppress the small scale noise. The uncertainties of a smoothed  $\kappa$  map are specified by the number density of source galaxies,  $n_g$ , and the smoothing aperture size  $\theta_G$ . van Waerbeke 2000 [26] shows that the noise can be approximated by a Gaussian distribution with RMS:

$$\sigma_{noise}^2 = \frac{\sigma_\epsilon^2}{4\pi\theta_G^2 n_g}, \quad (12)$$

where  $\sigma_\epsilon^2$  is the RMS amplitude of the source intrinsic ellipticity distribution.

To simulate a more realistic convergence map, we first smooth our convergence map with the Gaussian window.

We then add the noise resulting from intrinsic ellipticity of source galaxies using Eq.12. Following [27], we set  $\sigma_\epsilon = 0.4$ .

To investigate the effect of smoothing scale on our results, we adopt three different smoothing scale  $\theta_G = 0.5, 1$  and  $5$  arcmin. For  $n_g$ , we adopt two values:  $n_{g1} = 30 \text{ arcmin}^{-2}$  for upcoming surveys such as DES and  $n_{g2} = 100 \text{ arcmin}^{-2}$  for future more ambitious surveys.

## B. Minkowski Functionals

Minkowski Functionals provide morphological statistics for any given smoothed random field characterised by a certain threshold  $\nu$ . Compared with traditional power spectrum methods, MFs contain not only information of spatial correlation of a random field, but also information of topology and object shapes. For a  $\mathbb{R}^n$  field one can get  $n+1$  MFs  $V_i$ . Weak lensing convergence map is a two-dimensional field, thus 3 MFs can be defined, namely  $V_0$ ,  $V_1$ , and  $V_2$ .

For a smoothed field

$u(\mathbf{x})$  in a 2D space, we define the area  $Q_\nu$  and boundary  $\partial Q_\nu$  to be:

$$Q_\nu \equiv \{\mathbf{x} \in \mathbb{R}^2 | u(\mathbf{x}) > \nu\}, \quad \partial Q_\nu \equiv \{\mathbf{x} \in \mathbb{R}^2 | u(\mathbf{x}) = \nu\}.$$

Then, MFs can be written as follows:

$$V_0(\nu) = \int_{Q_\nu} d\Omega, \quad (13)$$

$$V_1(\nu) = \int_{\partial Q_\nu} \frac{1}{4} dl, \quad (14)$$

$$V_2(\nu) = \int_{\partial Q_\nu} \frac{1}{2\pi} \kappa_c dl. \quad (15)$$

$V_0$  is the area of  $Q_\nu$ ,  $V_1$  is the total boundary length of  $Q_\nu$  and  $V_2$  is the integrated geodesic curvature  $\kappa_c$  along the boundary.

We follow the method described in [21, 28] to calculate the MFs from the pixelated maps. On each grid, we calculate:

$$\mathcal{I}_0(\nu, p_j) = \Theta(u - \nu), \quad (16)$$

$$\mathcal{I}_1(\nu, p_j) = \frac{1}{4} \delta(u - \nu) \sqrt{u_{,x}^2 + u_{,y}^2}, \quad (17)$$

$$\mathcal{I}_2(\nu, p_j) = \frac{1}{2\pi} \delta(u - \nu) \frac{2u_{,x}u_{,y}u_{,xy} - u_{,x}^2u_{,yy} - u_{,y}^2u_{,xx}}{u_{,x}^2 + u_{,y}^2}, \quad (18)$$

where  $u_x, u_y$  are the two partial derivatives of  $u(\mathbf{x})$ . The numerical MFs of  $V_i$  can be computed by summing integrands over all pixels:

$$V_i(\nu) = \frac{1}{N_{pix}} \sum_{j=1}^{N_{pix}} \mathcal{I}_i(\nu, p_j), \quad (19)$$

In the above,  $\Theta$  is the Heaviside step function. For the bin width  $\Delta\nu$ , the delta function can be numerically calculated as follows:

$$\delta_N(\nu) = (\Delta\nu)^{-1} [\Theta(\nu + \Delta\nu/2) - \Theta(\nu - \Delta\nu/2)]. \quad (20)$$

Note that the numerical MFs, Eq. 19, is actually the surface density of Equations 13, 14 and 15. In what follows, we refer to both of them as MFs and notation  $V_i$ .

## IV. RESULTS

In Fig. 1, we show the MFs of surface density from our simulations. The MFs are plotted as functions of surface density in unit of mean surface density,  $\Sigma_{\text{mean}}$ . The overall shapes of MF curves of the  $f(R)$  and GR models are similar. However, the amplitude of MFs of the  $f(R)$  surface density map is higher at  $\Sigma/\Sigma_{\text{mean}} > 2$ . For the F6 case,  $V_0$  is  $\sim 10\%$  higher than that of GR model at  $\Sigma/\Sigma_{\text{mean}} \sim 3 - 5$ , while in denser regions ( $\Sigma/\Sigma_{\text{mean}} > 15$ ) the  $V_0$  of both models are almost identical. On the other hand, the difference in  $V_0$  between F5 and GR increases with  $\Sigma/\Sigma_{\text{mean}}$  and persists to larger density. At  $\Sigma/\Sigma_{\text{mean}} \sim 20$ , the  $V_0$  of F5 model is about 60% larger

than that of GR model. The  $V_1$  and  $V_2$  of F5 and F6 models show similar trends.

The apparent differences shown here reflect the environmentally dependent structure formation in universes with different gravity theories. As is shown in Ref. [29], compared with the GR universe, there are more massive halos and larger size voids in  $f(R)$  models because of the enhanced gravity in low density environments. As a result, the surrounding regions (including the filaments) of dark matter halos are denser in  $f(R)$  gravity than in GR. Therefore, in  $f(R)$  models,  $V_0$ , which represents the area of regions with density higher than certain threshold, is smaller than that of GR in the low density regions ( $\Sigma/\Sigma_{\text{mean}} < 1$ ), but is larger at relatively high density regions. For F6, in very high density regions, the chameleon screening ensures that both the gravity and MFs are similar to the results in GR.

The difference in  $V_1$  and  $V_2$  can also be explained in the similar way. However, unlike  $V_0$ ,  $V_1$  and  $V_2$  encode additional information on topology (which describes connectivity) of the  $\kappa$  map. As an example, the turn over trend in the lower panel of  $V_1$  indicates transition of the topology of  $\kappa$  map from the isolated halo dominated case to the voids dominated one.

In real observations, noise resulting from the intrinsic ellipticity distribution of galaxies contaminates the lensing  $\kappa$  map. Gaussian smoothing is usually adopted to suppress the noise; however, it will also mix the MFs of different density thresholds.

In Fig. 2, we show the MFs of the simulated  $\kappa$  maps without taking into account the noise. We apply smoothing to the map with different smoothing scales,  $\theta_G = 0.5, 1$  and  $5$ , respectively. Ref. [27] claimed that for cluster survey, the best smoothing scales is  $\sim 1$  arcmin. We find that the amplitudes of MFs at high density regions decrease significantly while the Poisson noises increase dramatically at the same region. This is because the smoothing procedure reduces total area of high density region. We conclude that a small smoothing scale is better for measuring MFs.

We show MFs of the  $\kappa$  map in Fig. 3 by taking into account the noise. Here we adopt two different noise cases,  $n_g = 30$  and  $n_g = 100$ , in order to investigate effects of different noise levels on our results. In the figure, we use a smoothing scale of  $1'$  and generate 100 maps using different background noises which sharing the same standard deviation  $\sigma_{\text{noise}}$ . The shaded regions show the standard deviation of MFs, which is an estimation of the noise level. We note that the noise map due to intrinsic galaxy shapes can be approximated with a Gaussian map, which migrate into MFs, thus suppressing the difference between  $f(R)$  and GR models. However, this effect is less important in dense regions ( $\kappa > 0.015$ ). Therefore, it is still possible to distinguish the F5, F6 and GR model in high density regime. It is also interesting to see that even for the higher noise level, where  $n_g = 30 \text{ arcmin}^{-2}$ , the difference among different gravity models is still much larger than the observational lensing noise, indicating that weak lensing MFs can be a powerful tool to distinguish the  $f(R)$  and GR models with upcoming galaxy surveys.

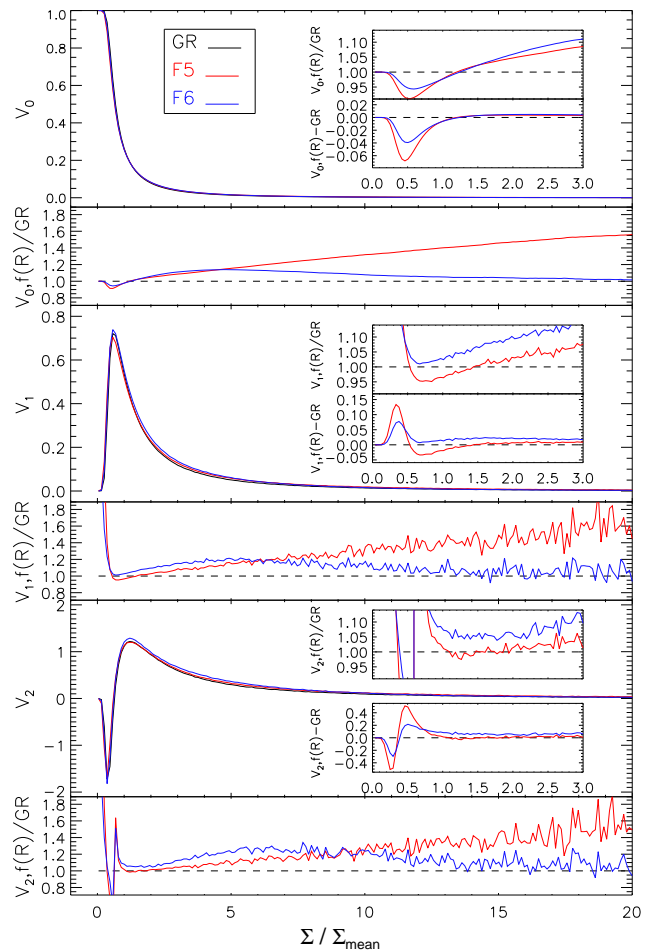


FIG. 1: The MFs of surface density maps as a function of surface density normalised to mean of the universe  $\Sigma_{\text{mean}}$  for our  $f(R)$  and GR simulations. The black solid, red dashed, and blue dotted lines represent result for GR, F5 and F6 simulation, respectively. Interior small figures each panel show the ratios between GR and  $f(R)$  simulations and the residuals as a function of surface density.

## V. SUMMARY

In this work, we make use of high-resolution  $f(R)$  (F5, F6) and GR simulations to generate mock lensing  $\kappa$  map by taking into account different noise levels. We find that due to environmentally dependent nature of  $f(R)$  gravity, the MFs of their  $\kappa$  maps show considerable deviation from the GR case. We also investigate the effect of lensing noise on our results, and find that while noise due to limited background source density induce pollution to the  $\kappa$  map, the difference between F5, F6 and GR gravity models can still be distinguished with a survey of  $\sim 3000 \text{ degree}^2$  area and with a background source number density  $n_g = 30 \text{ arcmin}^{-2}$ . Such a requirement can be achieved by upcoming lensing surveys. Our results hence suggest that the MFs of lensing  $\kappa$  map will be a powerful tool to study the nature of gravity in the future.

### Acknowledgement

We acknowledge support from the NSFC grant (No. 11303033, 11103011, 11373029, 11390372, 11403035, 11261140641), the Strategic Priority Research Program "The Emergence of Cosmological Structure" of the Chinese Academy of Sciences (No. XDB09000000), MPG partner Group family. RL acknowledges the support from Youth Innovation Promotion Association of CAS. JW acknowledges supports from the Newton Alumni Fellowship, the 1000-young talents program, the 973 program grant( No.

2013CB837900, 2015CB857005), the CAS grant(No. KJZD-EW-T01). LG acknowledges an STFC Advanced Fellowship, as well as the hospitality of the Institute for Computational Cosmology (ICC) at Durham University. The simulations in this work used the DiRAC Data Centric system at Durham University, operated by the ICC on behalf of the STFC DiRAC HPC Facility ([www.dirac.ac.uk](http://www.dirac.ac.uk)). This equipment was funded by BIS National E-infrastructure capital grant ST/K00042X/1, STFC capital grant ST/H008519/1, and STFC DiRAC Operations grant ST/K003267/1 and Durham University. DiRAC is part of the National E-Infrastructure.

- 
- [1] A. G. Riess, A. V. Filippenko, P. Challis, A. Clocchiatti, A. Diercks, P. M. Garnavich, R. L. Gilliland, C. J. Hogan, S. Jha, and R. P. Kirshner. *The Astronomical Journal*, 116(3):1009, (1998).
- [2] P. M. Garnavich, S. Jha, P. Challis, A. Clocchiatti, A. Diercks, A. V. Filippenko, R. L. Gilliland, C. J. Hogan, R. P. Kirshner, and B. Leibundgut. *The Astrophysical Journal*, 509(1):74, (1998).
- [3] T. Clifton, P. G. Ferreira, A. Padilla, and C. Skordis. *Physics Reports*, 513:1–189, (2012).
- [4] S. M. Carroll, A. De Felice, V. Duvvuri, D. A. Easson, M. Trodden, and M. S. Turner. *Physical Review D*, 71(6):063513, (2005).
- [5] J. Khoury and A. Weltman. *Physical Review D*, 69(4):044026, (2004).
- [6] A. C. Davis, E. A. Lim, J. Sakstein, and D. J. Shaw. *Physics Review D*, 85:123006, (2012).
- [7] J. Bhuvnesh, V. Vinu, and J. Sakstein. *The Astrophysical Journal*, 779:39, (2013).
- [8] L. Lombriser. *Annalen Phys.*, 526:259–282, (2014).
- [9] H. Oyaizu, M. Lima, and W. Hu. *Physical Review D*, 78:123524, (2008).
- [10] G.-B. Zhao, B. Li, and K. Koyama. *Physical Review D*, 83:044007, (2011).
- [11] B. Li, W. A. Hellwing, K. Koyama, G.-B. Zhao, E. Jennings, and C. M. Baugh. *Monthly Notices of the Royal Astronomical Society*, 428(1):743–755, (2013).
- [12] W. A. Hellwing, B. Li, C. S. Frenk, and S. Cole. *Monthly Notices of the Royal Astronomical Society*, 435:2806–2821, (2013).
- [13] K. R. Mecke, T. Buchert, and H. Wagner. *Astronomy and Astrophysics*, 288:697–704, (1994).
- [14] J. Schmalzing, M. Kerscher, T. Buchert, J. R. Primack, and A. Provenzale. Minkowski functionals in cosmology, n/a 1, 1996 1996.
- [15] J. Schmalzing and K. M. Gorski. *Monthly Notices of the Royal Astronomical Society*, 297:355–365, (1998).
- [16] J. Schmalzing, S. Gottber, A. A. Klypin, and A. V. Kravtsov. *Monthly Notices of the Royal Astronomical Society*, 309:1007–1016, (1999).
- [17] C. Hikage, J. Schmalzing, T. Buchert, Y. Suto, I. Kayo, A. Taruya, M. S. Vogeley, F. Hoyle, III Gott, J. R., and J. Brinkmann. *Publications of the Astronomical Society of Japan*, 55:911–931, (2003).
- [18] S. Codis, C. Pichon, D. Pogosyan, F. Bernardeau, and T. Matsumura. *Monthly Notices of the Royal Astronomical Society*, 435:531–564, (2013).
- [19] M. Kerscher, J. Schmalzing, T. Buchert, and H. Wagner. *Astronomy and Astrophysics*, 333:1–12, (1998).
- [20] A. Petri, Z. Haiman, L. Hui, M. May, and J. M. Kratochvil. *Physical Review D*, 88(12):123002, (2013).
- [21] J. M. Kratochvil, E. A. Lim, S. Wang, Z. Haiman, M. May, and K. Huffenberger. *Physical Review D*, 85(10):103513, (2012).
- [22] B. Li, G.-B. Zhao, R. Teyssier, and K. Koyama. *Journal of Cosmology and Astroparticle Physics*, 2012(01):051, (2012).
- [23] W. Hu and I. Sawicki. *Physical Review D*, 76:064004, (2007).
- [24] L. S., P. A. Abell, J. Allison, S. F. Anderson, and Andrew. Lsst science book, version 2.0, December 1, 2009 2009.
- [25] A. Refregier, A. Amara, T. D. Kitching, A. Rassat, R. Scaramella, J. Weller, and f. t. Euclid Imaging Consortium. Euclid imaging consortium science book, January 1, 2010 2010.
- [26] L. van Waerbeke. *Monthly Notices of the Royal Astronomical Society*, 313:524–532, (2000).
- [27] T. Hamana, M. Takada, and N. Yoshida. *Monthly Notices of the Royal Astronomical Society*, 350:893–913, (2004).
- [28] E. A. Lim and D. Simon. *Journal of Cosmology and Astroparticle Physics*, 01:048, (2012).
- [29] B. Li, G. B. Zhao, and K. Koyama. *Monthly Notices of the Royal Astronomical Society*, 421(4):3481–3487, (2012).

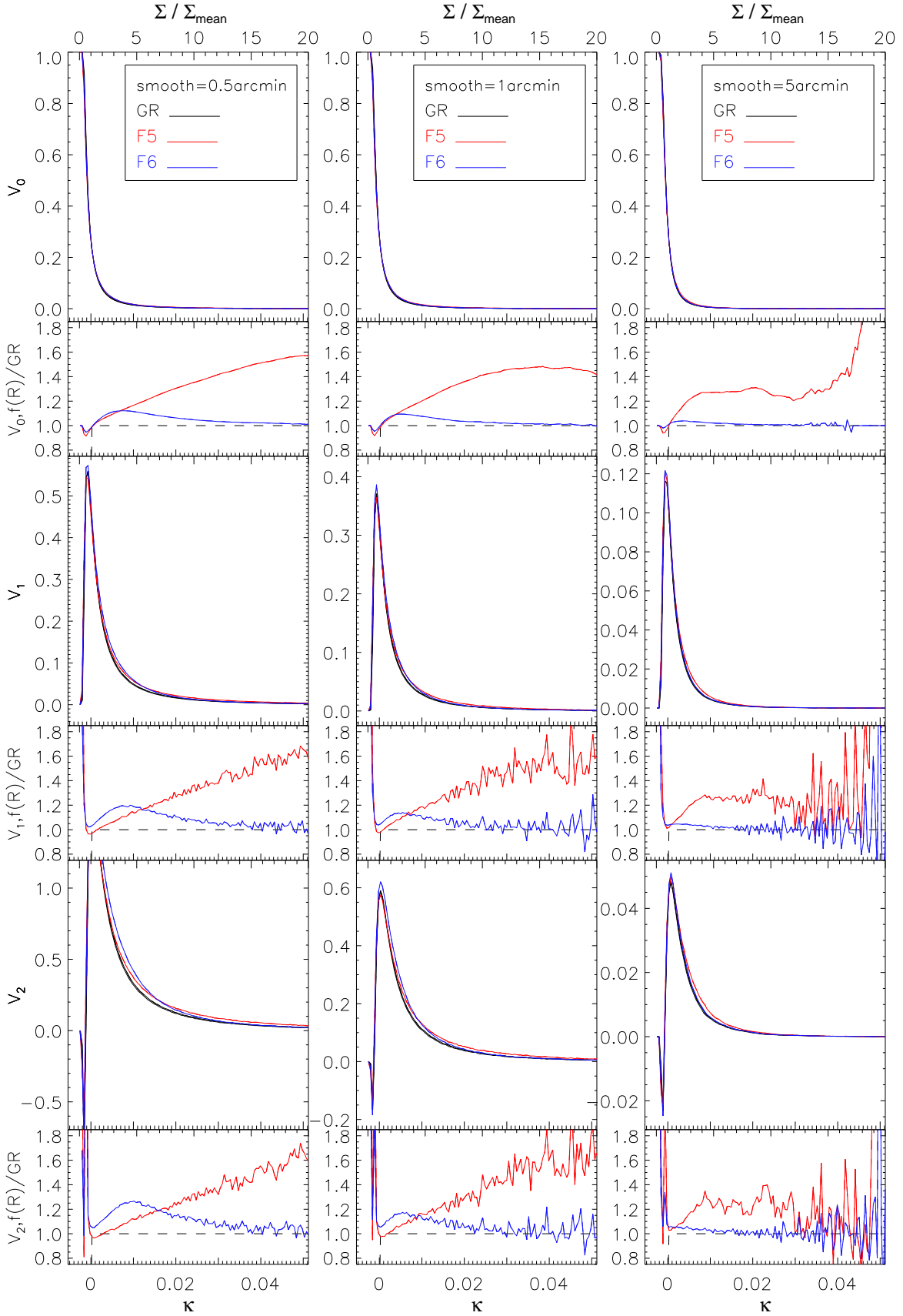


FIG. 2: The MFs of the noiseless  $\kappa$  maps as a function of  $\kappa$  (lower axis) and  $\Sigma/\Sigma_{mean}$  (upper axis). The black solid, red dashed, and blue dotted lines represent result of GR, F5 and F6 models respectively. The panels from left to right show results with different smoothing scales: 0.5', 1' and 5', respectively.

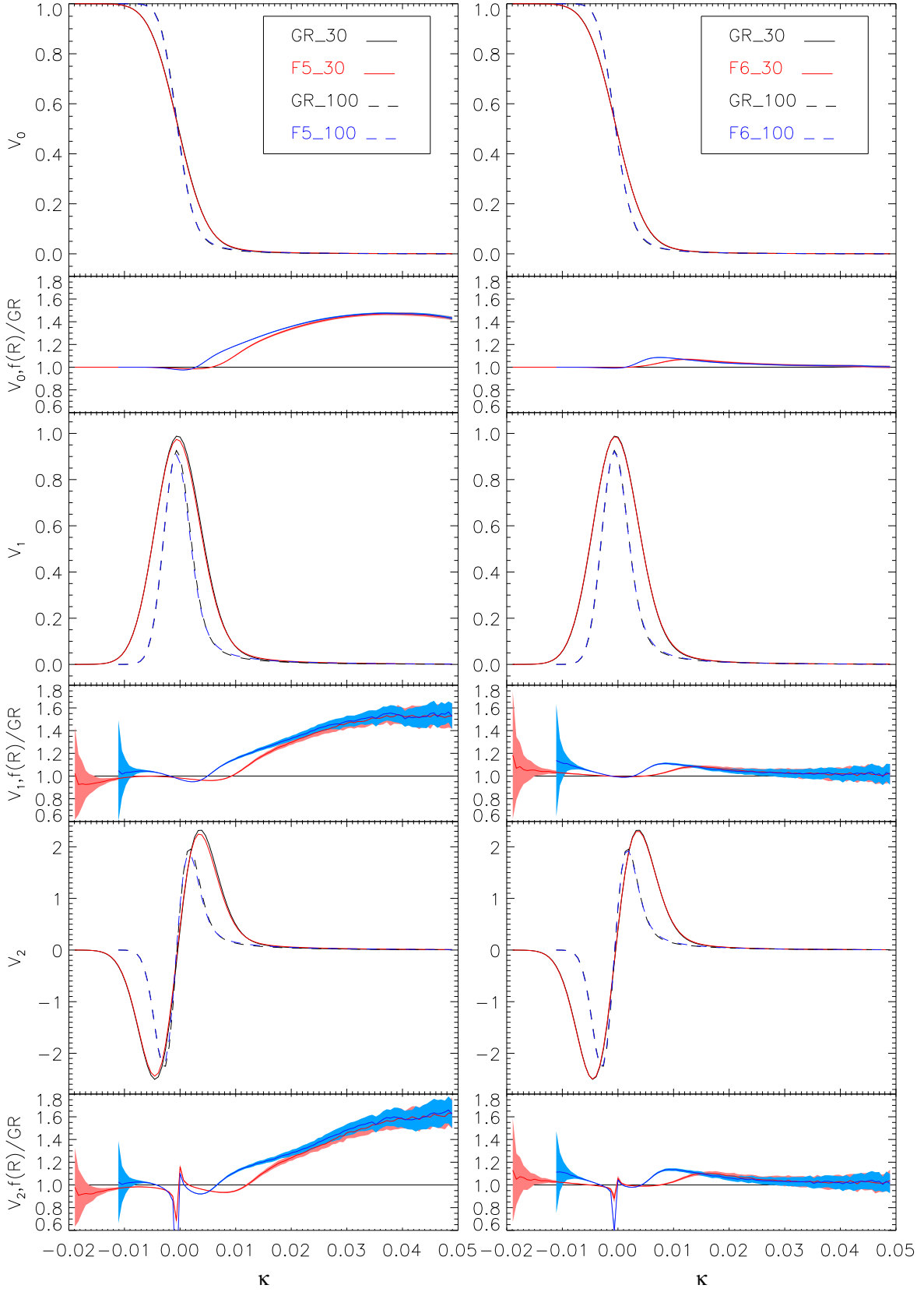


FIG. 3: Comparisons of the predicted MFs of lensing  $\kappa$  maps between the  $f(R)$  and GR simulations considering two different source number density,  $n_g = 30$  and  $n_g = 100$ . The left panel show comparison between F5 and GR models, while the right panel show comparison between F6 and GR models. The shaded regions show standard deviation of MFs from 100 mocked lensing maps.